JGR Oceans

RESEARCH ARTICLE
10.1029/2022JC019156

Ice Shelf Basal Melt Sensitivity to Tide-Induced Mixing Based on the Theory of Subglacial Plumes

J. Anselin[1,2], B. C. Reed[3], A. Jenkins[4], and J. A. M. Green[3]

[1]British Antarctic Survey, Cambridge, UK, [2]Department of Applied Mathematics and Theoretical Physics, University of Cambridge, Cambridge, UK, [3]School of Ocean Sciences, Bangor University, Menai Bridge, UK, [4]Department of Geography and Environmental Sciences, Northumbria University, London, UK

Abstract Tidal currents are known to influence basal melting of Antarctic ice shelves through two types of mechanisms: local processes taking place within the boundary current adjacent to the ice shelf-ocean interface and far-field processes influencing the properties of water masses within the cavity. The separate effects of these processes are poorly understood, limiting our ability to parameterize tide-driven ice shelf-ocean interactions. Here we focus on the small-scale processes within the boundary current. We apply a one-dimensional plume model to a range of ice base geometries characteristic of Antarctic ice shelves to study the sensitivity of basal melt rates to different representations of tide-driven turbulent mixing processes. Our simulations demonstrate that tides can either increase or decrease melt rates depending on the approach chosen to parameterize entrainment of ambient water into the turbulent plume layer, a process not yet well constrained by observations. A theoretical assessment based on an analogy with tidal bottom boundary layers suggests that tide-driven shear at the ice shelf-ocean interface enhances mixing through the pycnocline. Under this assumption our simulations predict a tide-induced increase in melt and freeze rates along the base of the ice shelf, with the strongest plume path-integrated effects for cold cavities (up to +400% in the realistic set up). An approximation is provided to account for this response in basal melt rate parameterizations that neglect the effect of tide-induced turbulent mixing.

Plain Language Summary Most of Antarctica's coastline is fringed by floating ice platforms called ice shelves. Many ice shelves are thinning through a process called basal melting. This ocean-driven process influences how much the Antarctic Ice Sheet is contributing to global sea level rise. A better understanding of the mechanisms that drive basal melting will therefore help to improve the accuracy of sea level projections. Basal melting is governed by a complex interplay between ocean conditions, the shape of the base of the ice shelf, and tides. Here we use a one-dimensional computer model to study how currents generated by tides influence basal melting through processes that occur close to the interface between the ice and the ocean. Our model predicts that tidal currents generate an increase in basal melting. However, we also show that the results are sensitive to assumptions made when representing the effects of tides in the computer code. Based on our model results we provide an expression that can be used to estimate the average effect of tidal currents on basal melt rates.

Key Points:

- Basal melt sensitivity to tide-induced shear at the ice-ocean interface is evaluated from one-dimensional plume simulations
- Tidal forcing enhances basal melting/freezing when tides are included in the entrainment formulation, and vice versa
- There is a quadratic relationship between the relative increase in net tidal melt rate and the ratio between tidal and plume velocities

Supporting Information:

Supporting Information may be found in the online version of this article.

Correspondence to:

J. A. M. Green,
m.green@bangor.ac.uk

Citation:

Anselin, J., Reed, B. C., Jenkins, A., & Green, J. A. M. (2023). Ice shelf basal melt sensitivity to tide-induced mixing based on the theory of subglacial plumes. *Journal of Geophysical Research: Oceans*, *128*, e2022JC019156. https://doi.org/10.1029/2022JC019156

Received 2 AUG 2022
Accepted 10 APR 2023

Author Contributions:

Conceptualization: J. Anselin
Data curation: J. Anselin
Formal analysis: J. Anselin
Methodology: B. C. Reed, A. Jenkins
Project Administration: J. Anselin
Software: A. Jenkins
Supervision: B. C. Reed, J. A. M. Green
Writing – original draft: J. Anselin
Writing – review & editing: B. C. Reed, A. Jenkins, J. A. M. Green

1. Introduction

Antarctic ice shelves—the floating tongues of ice that fringe most of the continent's coastline—are formed when glaciers reach the ocean and lose contact with the seabed. Satellite-derived observations have revealed that many ice shelves are experiencing thinning, caused primarily by ocean-induced ablation at their base (Jenkins et al., 2018; Paolo et al., 2015). This enhanced level of basal melting reduces the ice shelves' ability to restrain the seaward flow of grounded ice from the interior of the ice sheet (Gudmundsson et al., 2019), resulting in mass loss, and hence sea level rise, from the Antarctic Ice Sheet (AIS). Given the influence of ocean-driven melting on the rate at which the AIS is contributing to global sea level change (DeConto & Pollard, 2016), an improved representation of basal melting in numerical models has become an essential prerequisite for improving the reliability of sea level forecasting.

Ice shelf cavities are often classed as either "cold" or "warm" depending on the temperature of the water mass that dominates the sub-ice shelf circulation (Joughin et al., 2012). In cold cavities the circulation is driven either by dense high-salinity shelf water (HSSW) formed due to brine rejection from sea ice growth, or by Antarctic

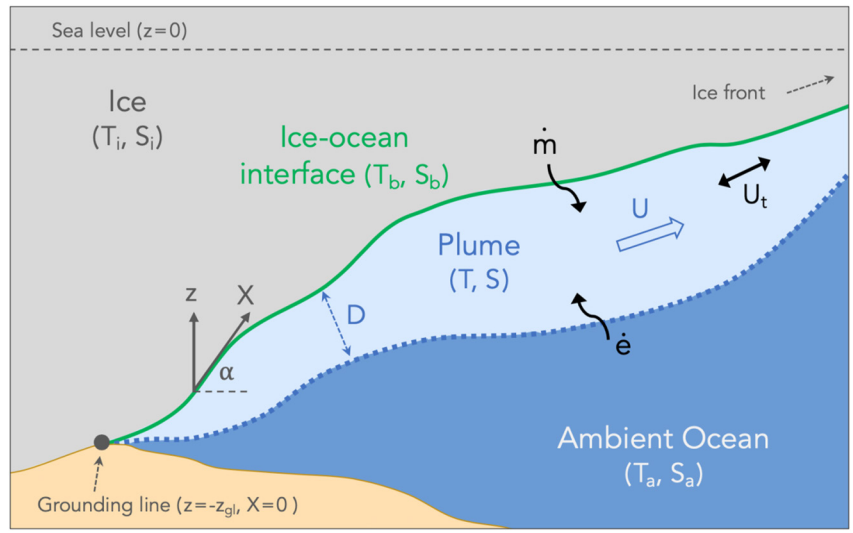

Figure 1. Schematic representation of the one-dimensional plume model of Jenkins (1991) used as a basis for this study, and adapted to incorporate the effect of tidal currents U_t. The meltwater plume (colored in light blue and characterized by its thickness D, depth-averaged temperature T, salinity S, and velocity U) is initiated at the grounding line ($z = -z_{gl}$, $X = 0$) and travels along the ice shelf base, following the path X. The ice draft geometry along the path of the plume is defined by a local slope $\sin\alpha = dz/dX$. The evolution of the plume is controlled by local entrainment of ambient water ($\dot{e}$) across the pycnocline (represented by the dashed blue line) and melting ($\dot{m}$) at the ice-ocean interface (marked in green). Note that while the seabed has been included in the schematic for illustration purposes, the influence of seabed geometry is ignored in the plume model.

Surface Water. Under warm ice shelves, modified Circumpolar Deep Water comes into contact with the ice base after having intruded onto the continental shelf. In both types of cavities, the release of fresh glacial meltwater into the saltier ocean leads to the creation of a buoyant meltwater flow that rises up the base of the ice shelf while mixing with ocean water in the cavity. The dynamics of this boundary current play an important role in regulating the exchange of heat across the ice-ocean interface, which subsequently controls the amount of melting along the base of the ice shelf (Hewitt, 2020). Due to the pressure dependency of the freezing point of seawater, the boundary current can reach a depth at which it becomes supercooled and forms marine ice, either directly at the ice base or through accretion of suspended frazil ice crystals (Craven et al., 2009; Lambrecht et al., 2007). This sub-ice shelf regime, characterized by melting in the vicinity of the grounding line and ice growth closer to the surface, is often referred to as "ice pump" (Lewis & Perkin, 1986).

Jenkins (1991) numerically described the dynamics of the buoyant flow of ice shelf water in a one-dimensional plume model (schematically represented in Figure 1). Subsequently, several studies have used variations of this conceptual framework to provide insight into the physical processes controlling basal melt (e.g., Bombosch & Jenkins, 1995; P. R. Holland & Feltham, 2006; Jenkins, 2011). However, fully resolving the oceanic boundary layer is computationally expensive, which limits the level to which boundary current dynamics can be captured in continental-scale coupled ice-ocean models. In the context of global sea level projections obtained from state-of-the-art ice sheet modeling simulations (e.g., DeConto & Pollard, 2016), the influence of basal melt on ice dynamics needs to be modeled without relying on ocean general circulation models. In these instances basal melt rates can be inferred from more or less complex parameterizations (Burgard et al., 2022; Favier et al., 2019).

To reduce computational complexity, tides are omitted in many ice shelf-ocean models (see e.g., Asay-Davis et al., 2017). As a result, their influence is not accounted for in parameterizations derived from these models. However, as described by Padman et al. (2018), tidal currents can affect basal melt through various mechanisms that can be categorized into two types: local processes influencing turbulent mixing within the ice shelf-ocean boundary current, and far-field processes that modulate the thermohaline properties of the water masses coming into contact with the ice base (e.g., sea ice motion, tidal rectification, cavity-scale vertical mixing). Studies using regional ocean models capable of explicitly simulating tides suggest that the *combined* effect of these processes is to increase the average basal melt rate under both cold and warm Antarctic ice shelves (Arzeno et al., 2014; Galton-Fenzi et al., 2012; Hausmann et al., 2020; Jourdain et al., 2019; Makinson et al., 2011; Mueller et al., 2012, 2018; Robertson, 2013). However, the *separate* effects of each tide-induced mechanism are

not as well understood. Addressing this gap in our understanding of the influence of tides would help to develop more effective parameterizations of tide-driven basal melting.

In this study, we focus on tide-driven turbulent mixing within the boundary current adjacent to the ice shelf-ocean interface. This mechanism has been suggested as the dominant process through which tidal currents impact basal melting under Filchner-Ronne Ice Shelf (Hausmann et al., 2020) and ice shelves in the Amundsen Sea sector (Jourdain et al., 2019). Rather than attempting to estimate absolute basal melt rates, our primary aim is to quantify the sensitivity of relative changes in melt rate to the representation of different tide-driven turbulent mixing processes. To this end, tides are incorporated into the traditional model of Jenkins (1991) (hereafter referred to as "the plume model"), and the model is applied to idealized and realistic ice shelf basal profiles. While there are limitations associated with the use of the plume model (as discussed in Section 4), its main advantages are that it is computationally inexpensive while still encapsulating the along-slope boundary current dynamics and its effects on local basal melt rates. Furthermore, one of the most advanced basal melt rate parameterizations for use in standalone ice sheet models, recently developed by Lazeroms et al. (2019; henceforth abbreviated as L2019), was derived from the same model. If tide-driven turbulent processes are shown to impact basal melt rates, the results from our simulations could potentially be used to improve the L2019 parameterization by accounting for these effects.

This paper is structured as follows: Section 2 describes the model set up and gives an overview of the simulations; Section 3 presents model results; Section 4 highlights model limitations, compares results with findings from previous studies, and discusses considerations for prescribing tide-induced basal melting in ice sheet models; Section 5 concludes by suggesting avenues for future research.

2. Methods

2.1. Plume Model Overview

2.1.1. Governing Equations Without Tides

The plume model considers the ocean within the ice shelf cavity as a two-layer system. The top layer (colored in light blue in Figure 1) represents the turbulent ice shelf-ocean boundary current, conceptualized here as a buoyant meltwater plume. The plume is characterized in terms of its spatially varying thickness D, velocity U, temperature T, and salinity S, and it is assumed to be turbulent throughout. The bottom layer (colored in darker blue in Figure 1) represents the ambient ocean, assumed to be stationary and well mixed. The ice shelf geometry, also assumed to be stationary, is described by a local slope $\sin\alpha = dz/dX$, with z being the vertical coordinate and X representing the along-slope distance. The plume is initiated at the grounding line before rising toward the ice front. On its upward path, it grows by entraining ambient ocean water (at rate $\dot{e}$) and it interacts with the ice-ocean interface (characterized by temperature T_b and salinity S_b) either through melting ($\dot{m} > 0$) or through freezing ($\dot{m} < 0$) depending on the temperature of the plume relative to the local freezing point at the interface. The melt and freeze rates are influenced by turbulent mixing of heat and salt across the plume, parameterized in the model through the heat and salt transfer velocities γ_T and γ_S. The positive buoyancy of the plume is counteracted by ice shelf basal drag, expressed as a function of a constant drag coefficient C_d (refer to Table S1 in Supporting Information S1 for model parameter values). Assuming steady-state flow, depth-averaged properties within the plume, and neglecting Coriolis effects, frazil ice formation, and tides, gives the following conservation equations for the fluxes of mass, momentum, heat, and salt, respectively:

$$\frac{d(DU)}{dX} = \dot{e} + \dot{m}, \tag{1}$$

$$\frac{d\left(DU^2\right)}{dX} = D\frac{\Delta\rho}{\rho_0} g\sin\alpha - C_d U^2, \tag{2}$$

$$\frac{d(DUT)}{dX} = \dot{e}\,T_a + \dot{m}\,T_b - \gamma_T\,(T - T_b), \tag{3}$$

$$\frac{d(DUS)}{dX} = \dot{e}\,S_a + \dot{m}\,S_b - \gamma_S\,(S - S_b). \tag{4}$$

The first term on the right-hand side of Equation 2 represents the plume's driving force due to buoyancy. It depends on the dimensionless density difference between the plume and the ambient ocean, calculated based on a linear equation of state:

$$\frac{\Delta\rho}{\rho_0} = \beta_S\,(S_a - S) - \beta_T\,(T_a - T), \tag{5}$$

where ρ_0 is a reference density, β_S is the haline contraction coefficient, β_T is the thermal expansion coefficient, and T_a and S_a are the ambient ocean temperature and salinity, respectively. The entrainment rate $\dot{e}$ is calculated as a linear function of the relative velocity between the boundary layer current and the speed of the surrounding waters. The ambient ocean is assumed to be motionless, resulting in the following expression:

$$\dot{e} = (E_0 \sin\alpha)\,U, \tag{6}$$

with E_0 an empirical constant and $\sin\alpha$ a factor introduced to account for the effect of slope on entrainment (Pederson, 1980). Three additional equations are required to close the system and solve for $\dot{m}$. They describe the balance of heat and salt fluxes at the ice-ocean interface and constrain the temperature of the ocean in contact with the ice base to be equal to the local depth-dependent freezing point:

$$\gamma_T\,(T - T_b) = \dot{m}\left[\frac{L}{c} + \frac{c_i}{c}\,(T_b - T_i)\right], \tag{7}$$

$$\gamma_S\,(S - S_b) = \dot{m}\,(S_b - S_i), \tag{8}$$

$$T_b = \lambda_1\,S_b + \lambda_2 + \lambda_3\,z_b, \tag{9}$$

where L is the latent heat of fusion of ice, c is the specific heat capacity of ocean water, c_i is the specific heat capacity of ice, T_i and S_i are the temperature and salinity of ice, and λ_1, λ_2, λ_3 are empirical constants used to express the seawater freezing point as a function of salinity and depth. The transfer velocities γ_T and γ_S can be expressed as a function of the interfacial friction velocity u_* (D. M. Holland & Jenkins, 1999), defined as the square root of the shear stress generated at the ice-ocean interface. The shear stress is commonly formulated in terms of the boundary layer current speed via a quadratic drag law. Within the one-dimensional plume model set up, this leads to the following friction velocity expression:

$$u_* = C_d^{1/2}\,U. \tag{10}$$

The heat and salt transfer velocities γ_T and γ_S can then be expressed as a linear function of the plume speed:

$$\gamma_T = \Gamma_T\,u_* = \Gamma_T\,C_d^{1/2}\,U, \tag{11}$$

$$\gamma_S = \Gamma_S\,u_* = \Gamma_S\,C_d^{1/2}\,U, \tag{12}$$

where Γ_T and Γ_S are the dimensionless turbulent transfer coefficients for heat and salt. Computing $\dot{m}$ based on the above set of equations results in melt rates proportional to the product of the speed and temperature of the plume (Jenkins, 2011).

2.1.2. Tidal Parameterization

Here, tidal currents are a source of velocity shear, and hence turbulence, at the ice-ocean interface. We assume that shear-driven turbulent mixing is generated throughout the tidal cycle independent of flow direction. Therefore, the root-mean-square (RMS) tidal current magnitude, U_t, calculated over a complete tidal cycle generates the same amount of turbulent mixing as a steady state oscillating current of the same magnitude. Based on this treatment of tidal velocity, and as recommended by Jenkins et al. (2010), a tidal factor was added to the velocity components when calculating the magnitude of the interfacial shear stress. This results in the following modified friction velocity formulation (see Derivation S1 in Supporting Information S1 for more detail):

$$u_* = C_d^{1/2}\left(U^2 + U_t^2\right)^{1/2}, \tag{13}$$

which in turn leads to these transfer velocity expressions:

$$\gamma_T = \Gamma_T u_* = \Gamma_T C_d^{1/2} \left(U^2 + U_t^2\right)^{1/2}, \tag{14}$$

$$\gamma_S = \Gamma_S u_* = \Gamma_S C_d^{1/2} \left(U^2 + U_t^2\right)^{1/2}. \tag{15}$$

Similarly, we incorporated the effect of tides on momentum flux into the model by adding a tidal factor to the frictional drag term in Equation 2 (see Derivation S1 in Supporting Information S1 for more detail). Neglecting momentum advection due to tides in line with the formulation implemented by Smedsrud and Jenkins (2004), the conservation equation for momentum then becomes:

$$\frac{d\left(DU^2\right)}{dX} = D\Delta\rho\, g \sin\alpha - C_d \left(U^2 + U_t^2\right)^{1/2} U. \tag{16}$$

Based on results from tidal model simulations suggesting that tides did not drive mixing beyond the pycnocline (Makinson, 2002), Smedsrud and Jenkins (2004) did not alter the entrainment rate expression when incorporating the effect of tides into their plume model. This approach supports one of the underlying assumptions of the plume model framework, in which entrainment is assumed to be driven solely by shear instability at the plume-ambient interface (and not by the production of turbulent kinetic energy (TKE) at the ice-ocean interface). Assuming tides to be barotropic, tidal currents then do not impact the vertical velocity gradient between the plume and the ambient ocean and should therefore not be included in the entrainment rate calculation. In contrast, most bulk layer models neglect the dynamical instability of the pycnocline and instead consider sources of TKE at the ice-ocean interface. As a result, ice shelf cavity models that employ such bulk mixed layer schemes to capture boundary current dynamics (e.g., D. M. Holland & Jenkins, 2001; Little et al., 2009) implicitly assume entrainment to be driven by TKE production at the ice-ocean interface. In this configuration, the addition of tides would impact the TKE budget of the plume layer, which would suggest the following modified entrainment rate formulation (see Derivation S2 in Supporting Information S1 for more detail):

$$\dot{e} = (E_0 \sin\alpha)\, U \left(1 + U_t^2/U^2\right)^{1/2}. \tag{17}$$

Tide forced simulations were performed based on Equations 6 and 17 to test the sensitivity of tide-induced melt rates to the two contrasting entrainment representations.

2.2. Experiments

We first applied the model to idealized ice shelf basal geometries with constant slope to gain a fundamental understanding of the effect of tide-induced turbulence on basal melting. Next, more realistic cross-sections were evaluated to quantify the effect of tides in configurations more representative of Antarctic ice shelves. Table 1 summarizes the model set ups applied in the "Idealized" and "Realistic" experiments.

2.2.1. Ice Shelf Basal Geometries

For the Idealized experiment, five basal geometries with constant slope were considered. The grounding line depths and basal slopes for each of these geometries are shown in Table 2 and were defined to encompass the range of values displayed by Antarctic ice shelves, based on the MEaSUREs BedMachine Antarctica data set (Morlighem et al., 2020). The Realistic experiment runs were conducted for vertical cross-sections along the eight cold cavity flowlines and four warm cavity flowlines shown in Figure 2, with ice shelf boundary and ice draft topography data again from BedMachine (Morlighem et al., 2020). These flowlines were selected by taking into account ice stream speed and tidal current speeds, and by ensuring that a wide range of Antarctic ice shelf geometries are being considered. Ice drafts were smoothed to reduce noise when computing melt rates. Given that the plume model code lacks the physics to cope with reverse basal slopes, sections with negative slope angles were replaced by a flat ice base portion.

2.2.2. Ambient Ocean Conditions

All model runs were performed under uniform ambient ocean conditions by applying constant vertical profiles of temperature and salinity. Cold cavity conditions were simulated with an ambient temperature of $T_a = -1.9°C$ which corresponds to the typical temperature of HSSW (Nicholls et al., 2009) and is in line with the thermal forcing applied by most other studies to have investigated the effect of tides on basal melting under cold ice shelves (e.g., Gwyther

Table 1
Summary of Experiments Detailing Ambient Ocean Temperature (T_a) and Along-Path Tidal Current Profile (U_t) Applied in Each Model Set Up

Experiment	Identifier	Model set up	T_a	U_t
Idealized	IC0	Cold/control	−1.9°C	Zero
	IC1	Cold/tide forced (tr only)	−1.9°C	Constant
	IC2	Cold/tide forced (tr + dr)	−1.9°C	Constant
	IC3	Cold/tide forced (tr + dr + e)	−1.9°C	Constant
	IW0	Warm/control	−1.0°C	Zero
	IW1	Warm/tide forced (tr only)	−1.0°C	Constant
	IW2	Warm/tide forced (tr + dr)	−1.0°C	Constant
	IW3	Warm/tide forced (tr + dr + e)	−1.0°C	Constant
Realistic	RC0	Cold/control	−1.9°C	Zero
	RC1	Cold/tide forced (tr only)	−1.9°C	Spatially varying
	RC2	Cold/tide forced (tr + dr)	−1.9°C	Spatially varying
	RC3	Cold/tide forced (tr + dr + e)	−1.9°C	Spatially varying
	RW0	Warm/control	−1.0°C	Zero
	RW1	Warm/tide forced (tr only)	−1.0°C	Spatially varying
	RW2	Warm/tide forced (tr + dr)	−1.0°C	Spatially varying
	RW3	Warm/tide forced (tr + dr + e)	−1.0°C	Spatially varying

Note. For tide forced set ups, (tr + dr + e) means that tides were added to the transfer velocity expressions (as per Equations 14 and 15), to the plume momentum equation (as per Equation 16) and to the entrainment rate expression (as per Equation 17); (tr + dr) means that tides were added to the transfer velocities and to the plume momentum equation but omitted from the entrainment parameterization; (tr only) means that tides were only added to the transfer velocities. The tide forced runs in the Realistic experiment were performed by specifying spatially varying RMS tidal current values derived from CATS2008.

et al., 2016; Hausmann et al., 2020; Mueller et al., 2018). For warm cavities we used $T_a = -1.0$°C, following L2019. In all set ups the ambient salinity was $S_a = 34.65$ psu, again as per the quantity applied by L2019. While in reality salinity varies depending on the water mass ventilating the cavity, we feel that this simplification is justified since salinity has been shown to have limited control on melt rates compared with thermal forcing (P. R. Holland et al., 2008).

2.2.3. Tidal Currents

A constant RMS tidal current speed of 0.20 m s^{-1} was applied in the tide forced runs of the Idealized experiment. This value corresponds to the upper bound of the X-averaged tidal current speed applied to the Realistic geometries (see Figure 6). In the Realistic experiment, we specified spatially varying tidal current magnitudes along the plume path in order to simulate varying degrees of tide-induced velocity shear at the ice-ocean interface. The RMS tidal current speeds were obtained from the regional barotropic tide model CATS2008 (Circum-Antarctic Tidal Solution version 2008, an update to the model described by Padman et al. (2002)) and calculated as:

$$U_t = \sqrt{\left\langle \left(\frac{U_b}{h}\right)^2 + \left(\frac{V_b}{h}\right)^2 \right\rangle}, \tag{18}$$

where U_b and V_b are orthogonal components of depth-integrated volume transport obtained from CATS2008 by accounting for all tidal constituents in the model (M_2, S_2, N_2, K_2, K_1, O_1, P_1, Q_1, M_f, M_m), and h is the local water column thickness from BedMachine Antarctica data (Morlighem et al., 2020). The angle brackets mark temporal averaging over a 30-day period (to capture two complete spring-neap cycles and one complete M_2-N_2 beat cycle).

3. Results

3.1. Model Behavior for Idealized Basal Geometries

Adding tides into the model based on the modified formulations of turbulent transfer velocities, conservation of momentum, and entrainment rate (tr + dr + e) acts to speed up the plume flow for the Idealized reference

Table 2
Ice Shelf Basal Geometries for Which the Plume Model Was Evaluated

Experiment	Geometries	z_{gl} (m)	z_{if} (m)	Slope	$\overline{\sin \alpha}$
Idealized	Reference	−1,000	0	Constant	0.002
	Deep	−2,500	0	Constant	0.002
	Shallow	−500	0	Constant	0.002
	Steep	−1,000	0	Constant	0.01
	Flat	−1,000	0	Constant	0.001
Realistic	Larsen	−520	−139	Varying	0.002
	Talutis (Ronne)	−1,273	−122	Varying	0.002
	Rutford (Ronne)	−1,466	−200	Varying	0.002
	Institute (Ronne)	−1,002	−258	Varying	0.001
	Support Force (Filchner)	−1,188	0	Varying	0.002
	Amery	−2,357	−200	Varying	0.004
	MacAyeal (Ross)	−707	−287	Varying	0.001
	Mercer (Ross)	−798	−169	Varying	0.001
	Thwaites	−571	−58	Varying	0.01
	Dotson	−1,183	−206	Varying	0.01
	Abbot	−353	0	Varying	0.004
	Cosgrove	−263	−258	Varying	0.0002

Note. z_{gl} denotes grounding line depth, Z_{if} ice draft at the ice front, and $\overline{\sin \alpha}$ refers to the ice shelf basal slope averaged along the plume path X. See Figures 3 and 5 for visual representations of the geometries.

configuration under both cold and warm conditions (*cf.* solid green lines with dashed-dotted black lines in Figures 3b and 3f, respectively). As expected based on the positive correlation between melt rate and boundary current speed (P. R. Holland et al., 2008), this translates into increased melt rates (Figures 3d and 3h). In the cold cavity set up, both melting (positive $\dot{m}$ values) and freezing (negative $\dot{m}$ values) increase with the addition of tides. This can be attributed to a strengthening of the ice pump circulation: more melting at depth means more melt-water produced, which decreases the temperature of the plume (*cf.* solid green line with dashed-dotted black line for $X > \approx 250$ km in Figure 3c). In turn, the decrease in thermal driving results in an enhanced rate of freezing. The increase in melt rate averaged over the melting portion of the plume path is larger than the averaged increase in freeze rate, resulting in a net melt rate increase over the plume path (Figure 4). Under warm cavity conditions no marine ice forms along the plume path. In this melt-only regime, the addition of tides results in an increase in plume temperature and melting at every point along the plume path (Figure 3h).

When incorporating tidal effects into the model without modifying the entrainment scheme (tr + dr), the direction of the tide-induced melt response is reversed. Compared with the simulations without tides, the speed of the plume is now reduced, resulting in a decrease in melt and freeze rates along the plume path (*cf.* solid orange lines with dash-dotted black lines in Figure 3). Regardless of the treatment of entrainment, the melt rate sensitivity to tides is greatest where the plume speed without tides (referred to in the following as "thermohaline-only" plume speed) is lower relative to the applied 0.20 m s^{-1} tidal current speed (dashed gray line in Figures 3b and 3f), as this corresponds to the section of the plume track where tidal currents dominate the flow. Similar behaviors are obtained for the four remaining constant slope geometries (not shown).

Figure 4a illustrates the relative effect of tidal currents on melt rates averaged over the entire plume path, as a function of grounding line depth and basal slope. The blue circles show the results for cold cavity ambient conditions and the red circles represent the warm cases, each evaluated with a constant 0.20 m s^{-1} RMS tidal current speed. For the purpose of this discussion, the size of the circles relative to each other is more important than their absolute size, as the latter would have varied if a different tidal current magnitude had been applied. Comparing the blue and red circles for each grounding line depth/basal slope combination indicates that the relative effect of tides on melt rates is stronger for cold conditions (the blue circles are larger than the red circles).

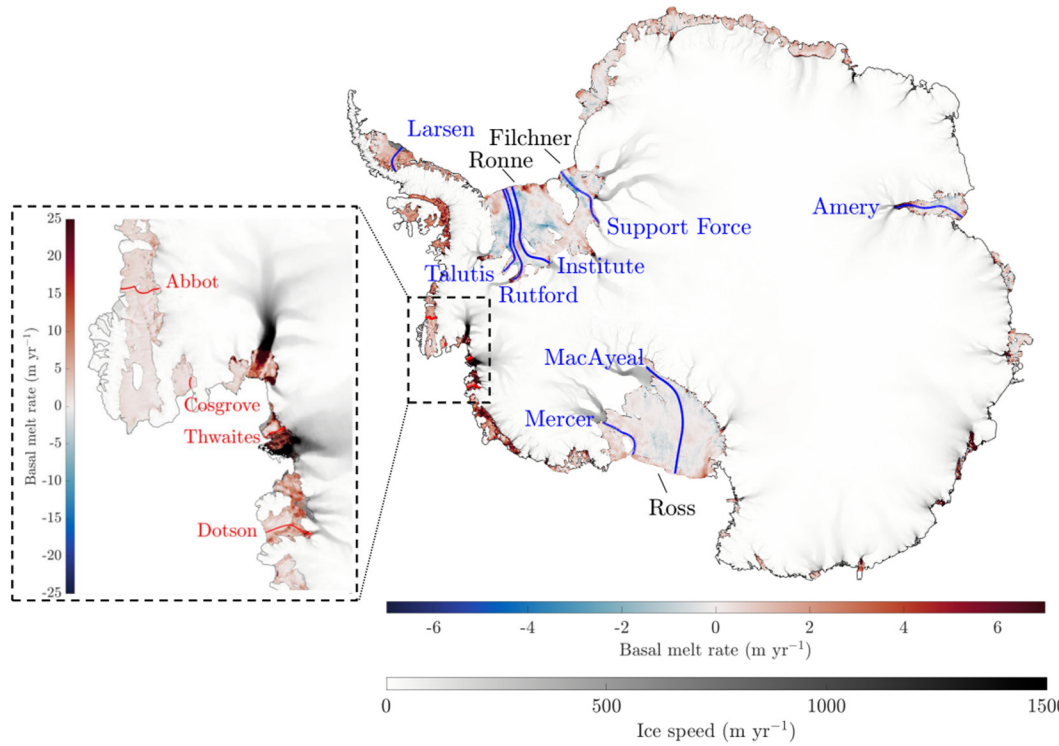

Figure 2. Map showing the Antarctic Ice Sheet and plume paths prescribed in the Realistic experiment. The modeled flowlines along cold cavity ice shelves are marked in blue and include the Filchner-Ronne Ice Shelf (Talutis, Rutford, Institute, and Support Force ice streams), Ross Ice Shelf (Mercer and MacAyeal ice streams), and the Larsen and Amery Ice Shelves. Modeled warm cavity flowlines are marked in red and include Abbot, Cosgrove, Thwaites, and Dotson Ice Shelves. The ice sheet background color indicates ice speed (Mouginot et al., 2012, 2017; Rignot et al., 2011) and the ice shelf background color shows basal melt rates derived from 2010 to 2018 satellite data (Adusumilli et al., 2020a).

This can be attributed to the weaker thermohaline-only plume circulation in the cold regime (*cf.* dash-dotted black line in Figure 3b with dash-dotted black line in Figure 3f), explained by the positive correlation between boundary current velocity and ambient ocean temperature (P. R. Holland et al., 2008; Jenkins, 2021). The weaker plume flow under cold conditions translates into an increased relative difference between the tidal current speed and plume speed such that the tidal currents are more likely to dominate the flow. Likewise, assuming the same basal slope, the sensitivity to tides decreases as the grounding line depth increases. Similarly, comparing the thermohaline-only plume speed under a steep ice base with that under a flat ice base (not shown) explains why, for the same grounding line depth, the flat ice shelf geometry is more sensitive to tides. Furthermore, as shown in Figure 4b, for a fixed grounding line depth the relative change in melt rate due to tides decays exponentially with basal slope, with a more pronounced response for cold conditions.

3.2. Model Behavior for Realistic Basal Geometries

The results obtained for the basal cross-sections along the 12 flowlines presented in Figure 2 are generally in line with trends described for the Idealized configurations, that is, with tidal effects incorporated into the entrainment rate expression (tr + dr + e), the inclusion of tides into the model acts to speed up the plume circulation, increase the plume temperature (along melting portions of the plume path), and increase melt and freeze rates. Conversely, when the entrainment law is left unchanged (tr + dr), the simulated plume circulation slows down with an associated reduction in plume temperature and melt rates. These effects can be seen in Figures 5b–5h, for the basal geometries along the flowlines of Talutis ice stream on Ronne ice shelf (cold cavity) and Abbot ice shelf (warm cavity). The model outputs for the remaining 10 flowlines display similar behaviors (not shown).

In contrast to the uniform tidal current applied in the Idealized simulations, spatially varying tidal current magnitudes were applied along each of the Realistic basal geometries (see dashed gray lines in Figures 5b and 5f for

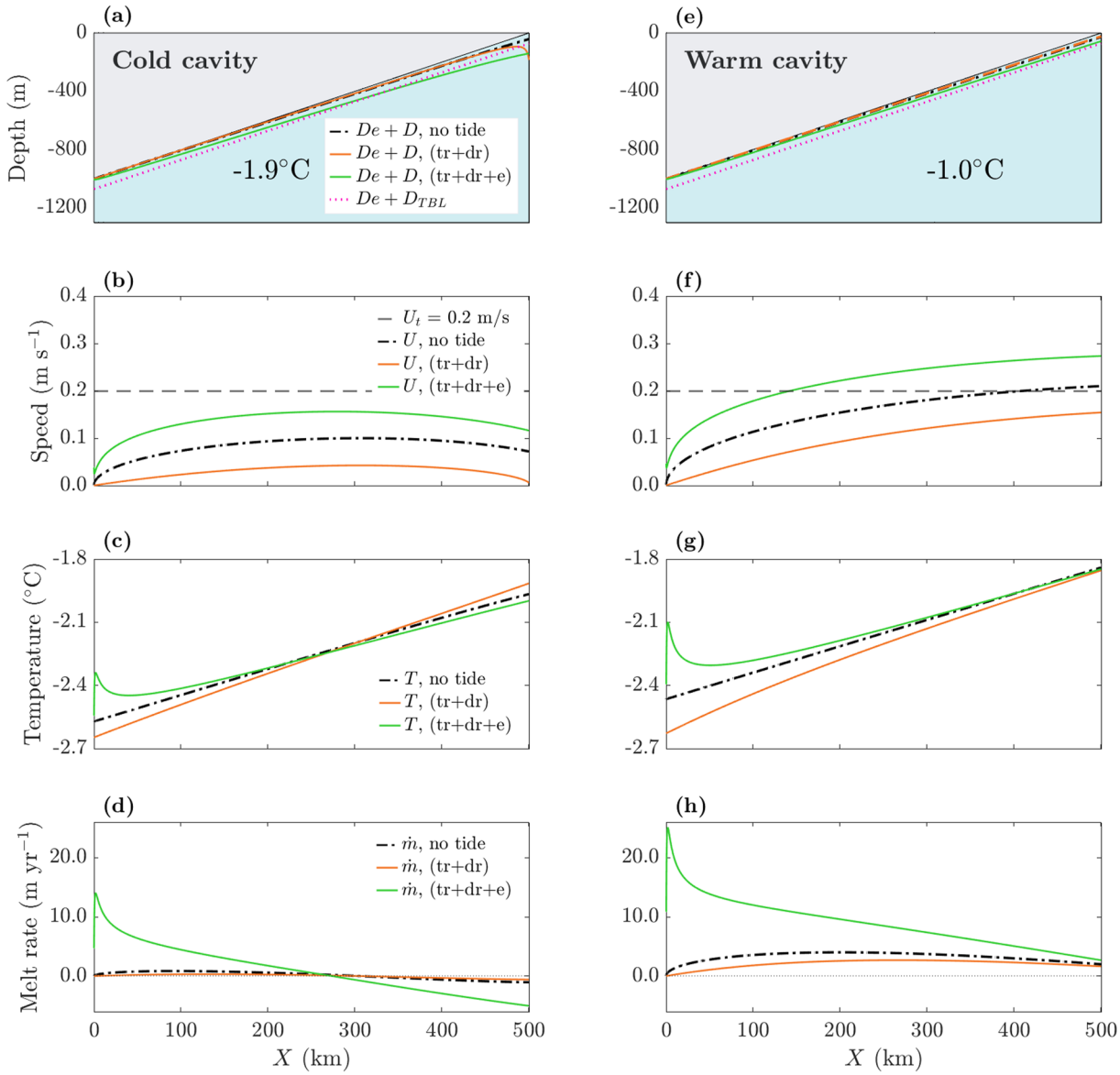

Figure 3. Simulated plume depth and theoretical tidal boundary layer depth (a and e), plume speed (b andf), plume temperature (c and g), and basal melt rate (d, h) along the plume path for the constant slope Idealized reference geometry under cold ambient conditions (a–d), and warm ambient conditions (e–h). The dash-dotted black lines represent the simulation without tides. The solid orange lines show the results obtained when incorporating tides into the plume model, neglecting the effect of tides on entrainment velocity (simulations IC2 and IW2 in Table 1). The solid green lines were obtained by incorporating the effect of tides into the entrainment expression (IC3 and IW3 in Table 1). All tide forced results are based on a uniform tidal current speed of 0.20 m s^{-1} specified along the entire plume path (gray dashed lines in panels (b and f)). The theoretical boundary layer depth was calculated based on Equation 19 with a semi-diurnal tidal frequency.

a visualization of the tidal current magnitudes applied to the flowlines along Talutis and Abbot). In terms of the resulting along-path variability of tide-induced effects, the influence of tides on circulation strength and melt rates is most pronounced along sections where the tidal current magnitude is largest relative to the thermohaline-only plume speed (Figure S1 in Supporting Information S1). The thermohaline-only plume speed is influenced by the steepness of the ice base via the slope-dependent buoyancy force, which acts to accelerate the plume flow. This implies that the tide-induced melt rate variability along the plume path is not just determined by variations in tidal current speed, but also by variations in basal slope.

The influence of X-averaged tidal current speed on melt rate is highlighted in Figure 6. Here the flowlines have been presented in descending order based on their X-averaged RMS tidal current magnitude. Consequently, comparing the horizontal position of the green and orange dots in the upper rows of Figure 6b to those in the

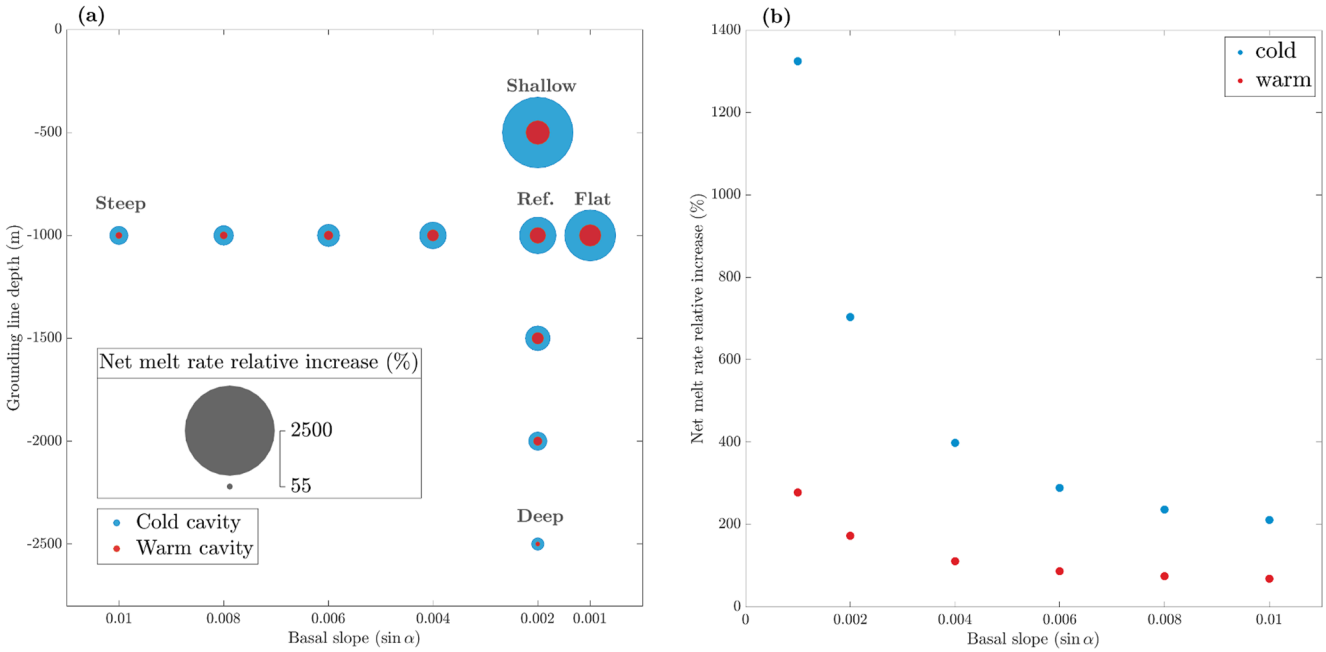

Figure 4. Percentage increase in net melt rate due to tides (calculated as $\left(\left(\overline{m}_{tideforced} - \overline{m}_{notide}\right)/\overline{m}_{notide}\right) \times 100$, where the overbar signifies averaging along X), (a) for different grounding line depth (y-axis) and basal slope (x-axis) configurations, and (b) as a function of basal slope only for a grounding line depth of −1,000 m. Tide forced melt rates were obtained from simulations IC3 and IW3 (see Table 1), with a constant 0.20 m s^{-1} tidal current speed specified along the plume path. In panel (a) the circle size indicates the magnitude of the relative increase in net melt rate.

bottom rows indicates that, irrespective of the treatment of tide-induced entrainment, the effect of tidal currents on basal melt rates appears to be strongest for flowlines experiencing the most intense tides (Filchner-Ronne and Larsen). The effect of tides on melt rates are found to be negligible for X-averaged tidal current speeds less than 0.020 m s^{-1} (Amery, Thwaites, Dotson). However, it is worth reiterating that our simulations only capture the effects of tides on the ice shelf-ocean boundary current. Therefore, while our model indicates minimal melt rate modulations for some of the flowlines, other tidal mechanisms like for example, cavity-scale vertical mixing could hypothetically influence melt rates. It is also clear from Figure 6b that the magnitude of the tide-induced melt rate difference is larger when tides are incorporated into the entrainment rate expression.

Based on the flowlines considered in this study, cold Antarctic ice shelves appear more sensitive to the effect of tides (Figure 6). This observation holds for the two entrainment related assumptions considered here, and it can be attributed to three main factors. First, some of the largest cold ice shelves around Antarctica are located in regions where tidal currents happen to be strongest (e.g., Filchner-Ronne and Larsen, see Figure 6a). Second, as mentioned in Section 3.1, the lower ambient ocean temperature under cold ice shelves leads to slower plume speeds, which results in a larger proportion of the plume path over which tidal currents can dominate the circulation. Third, the flowlines along warm ice shelves like for example, Thwaites and Dotson tend to have steeper average basal slopes (see Table 2), which, as explained above, leads to a lower sensitivity to tide-induced effects.

3.3. Evaluation of the Entrainment Rate Formulation in the Presence of Tides

As shown in Figure 6b, incorporating the effect of tides into the model results in either an increase or a decrease in basal melting, depending on the approach chosen to account for the effect of tides on the entrainment process. Leaving the entrainment law unmodified compared to the set up without tides (Equation 6) implies that tide-induced shear, and hence turbulence, created at the ice-ocean interface does not drive entrainment. Since the heat source to fuel basal melt comes from entrainment of ambient waters, no additional heat is being supplied to the plume. In this configuration the dominant effect of tide-induced shear is enhanced frictional drag, leading to a plume speed reduction and an associated decrease in steady state melt rate. In contrast, incorporating entrainment driven by TKE production at the ice-ocean interface (as per Equation 17) results in additional heat available, explaining the simulated increase in melt rates. To evaluate which of these two contrasting representations of the entrainment mechanism would be more suitable in the context of this study, we compared the plume thickness (D)

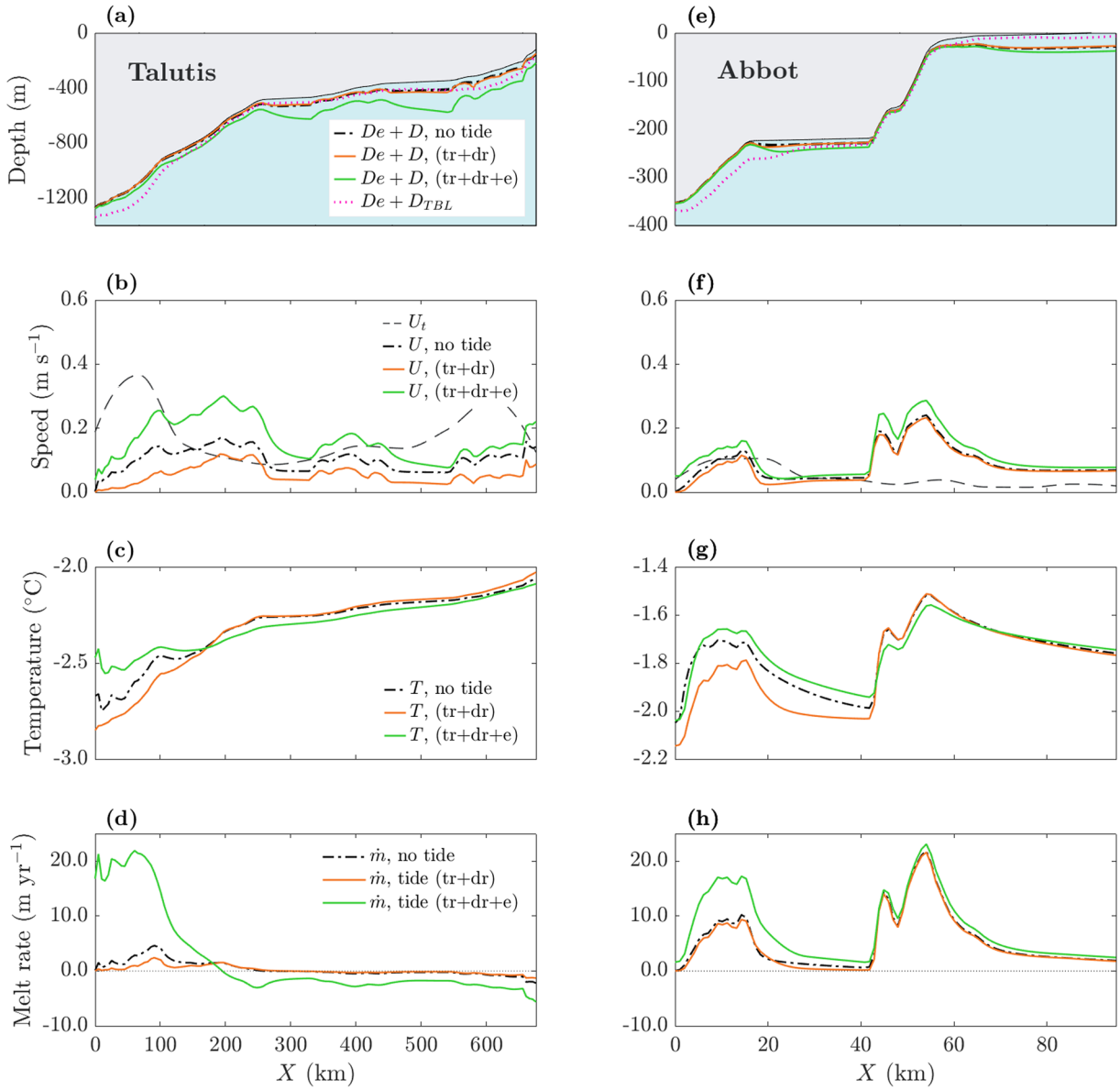

Figure 5. Simulated plume depth and theoretical tidal boundary layer depths (a and e), plume speed (b and f), plume temperature (c and g), and basal melt rate (d and h) along the plume path for two realistic ice base geometries representative of a cold ice shelf (left-hand column, Talutis Ice Stream on Filchner-Ronne Ice Shelf) and of a warm ice shelf (right-hand column, Abbot Ice Shelf). See Figure 2 for ice shelf locations and Table 2 for basal geometry details. The dash-dotted black lines represent the simulations without tides. The solid orange lines show the results obtained when incorporating tides into the plume model, neglecting the effect of tides on entrainment velocity (simulations RC2 and RW2 in Table 1). The solid green lines were obtained by incorporating the effect of tides into the entrainment expression (RC3 and RW3 in Table 1). The gray dashed lines in panels (b and f) show the tidal current speed applied along the plume path. The theoretical tidal boundary layer depth was calculated as per Equation 19 with a semi-diurnal tidal frequency.

obtained from our simulations without tides with a theoretical tidal boundary layer thickness (D_{TBL}). The rationale behind this analysis was that, if $D_{TBL} < D$, it would suggest that tides do not enhance mixing beyond the base of plume layer, and that the entrainment parameterization should not include a tidal contribution. On the other hand, if $D_{TBL} > D$, it would suggest that tide-induced mixing can entrain ambient water into the plume layer, supporting the addition of a tidal factor into the entrainment rate expression. Drawing on an analogy between ice shelf meltwater plumes and tidal bottom boundary layers of shelf seas, and ignoring the effects of Earth rotation and stratification to remain aligned with the plume model set up, D_{TBL} was calculated as (Bowden, 1978):

$$D_{TBL} = \frac{C_d^{1/2}\, U_t}{\omega}, \tag{19}$$

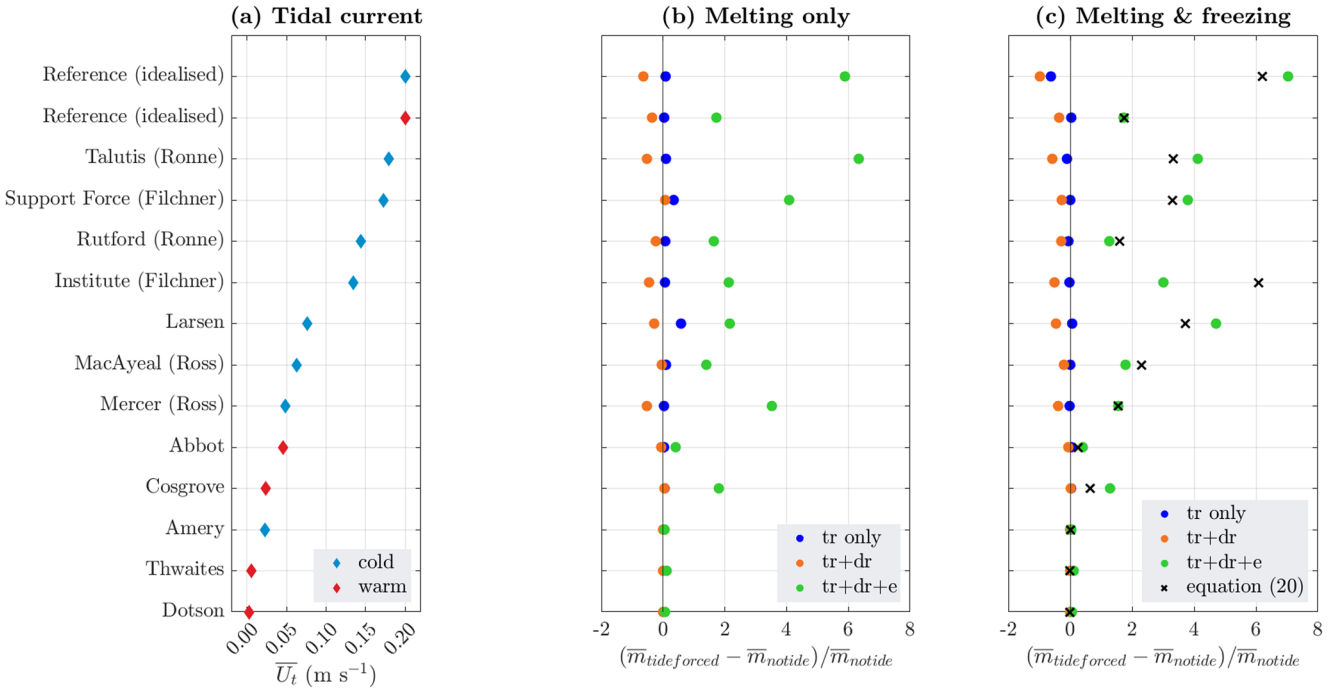

Figure 6. *X*-averaged root-mean-square tidal current (a), relative change in melt rate due to tides (calculated as $(\overline{m}_{tideforced} - \overline{m}_{notide})/\overline{m}_{notide}$, where the overbar signifies averaging along *X*) for sections along the flowline where $\dot{m}$ is positive (b), and relative change in net melt rate due to tides averaged along the entire plume path (c), for the Idealized constant slope reference geometry, and for the Realistic flowline geometries drawn in Figure 2. In panels (b and c), blue dotes indicate results obtained from model simulations IC1, IW1, RC1, and RW1; orange dots show results from runs IC2, IW2, RC2, and RW2; green dots were obtained from runs IC3, IW3, RC3, and RW3 (refer to Table 1 for a description of each simulation set up). The black crosses in (c) show the estimated increase in melt rate due to tides obtained from the tide-induced melt rate approximation described by Equation 20.

where ω is the tidal frequency. Setting ω to $2\pi/(3{,}600 \times 12.42)$ for locations with dominant semi-diurnal tides and $2\pi/(3{,}600 \times 23.9)$ for diurnal tides and comparing D and D_{TBL} along the plume path for each of the Realistic geometries shows that the tidal boundary layer depth exceeds the plume depth along the majority of the ice base. This is illustrated in Figure 5a for Talutis and in Figure 5e for Abbot. Similar results were obtained for the Idealized reference geometry under both cold and warm ambient conditions (Figures 3a and 3e). The *X*-averaged values of D_{TBL} exceed the *X*-averaged values of D for most of the flowlines considered in our Realistic experiment (see Figure A1 in the Appendix A). Exceptions to this include ice shelves experiencing very low tidal currents (Dotson, Thwaites, Amery). Bearing in mind that this comparative analysis is based on turbulence theory rather than in-situ observations of the actual physical processes, the findings described above suggest that, at least in terms of plume path-integrated values, tidal currents influence mixing beyond the depth of the plume base. This provides support for incorporating tides into the entrainment process parameterization as per Equation 17.

3.4. Quantification of the Effect of Tide-Induced Mixing on Basal Melt Rates

The relative effect of tide-driven turbulent mixing predicted by the plume model was parameterized by deriving an estimate of the tide-induced plume path-integrated (i.e., *X*-averaged) melt rate as a function of the ratio between *X*-averaged tidal velocity and thermohaline-only plume speed. To this purpose, a quadratic regression model was applied to melt rates obtained from the Idealized and Realistic plume simulations (Figure 7). An additional data point equal to (0; 0) was included to represent the control case without tides. Based on this analysis, the following representation of the effect of tide-driven turbulence on basal melt rate was deduced:

$$\overline{m}_{tideforced} = \overline{m}_{notide} \times \left(1 + 1.10\left(\overline{U_t}/\overline{U}\right)^2 - 0.06\,\overline{U_t}/\overline{U}\right), \tag{20}$$

where $\overline{m}_{tideforced}$ is the *X*-averaged melt rate accounting for the effect of tide-induced turbulent mixing, $\overline{m}_{notide}$ is the *X*-averaged melt rate obtained from a model or parameterization that does not incorporate tidal effects

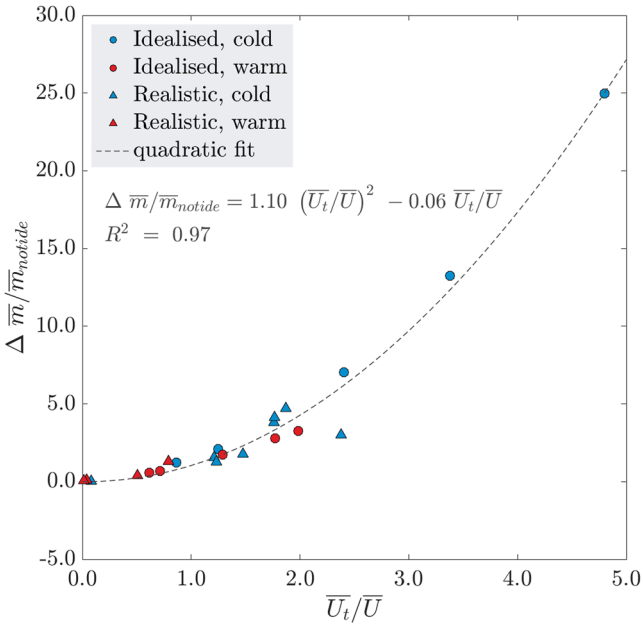

Figure 7. Relative difference in net melt rate due to tides, calculated as $\Delta\ \overline{m}/\overline{m}_{notide} = \left(\overline{m}_{tide\,forced} - \overline{m}_{notide}\right)/\overline{m}_{notide}$ (with overbars signifying averaging along X), versus the ratio of X-averaged root-mean-square tidal current speed to X-averaged thermohaline-only plume speed for the five Idealized geometries (Table 2) and for the 12 Realistic flowlines (Figure 2). Tide forced melt rates were obtained from simulations IC3, IW3, RC3, and RW3, in which the effect of tides on entrainment is included (see Table 1).

(e.g., L2019), $\overline{U_t}$ is the X-averaged RMS tidal current magnitude, and $\overline{U}$ is the X-averaged thermohaline-only plume speed. As further discussed in Section 4, this result must be considered with caution due to the limited data set from which it was derived and due to modeling simplifications (e.g., fixed ambient ocean salinity across all cold cavities). These modeling choices are deemed acceptable for the purpose of evaluating the relative importance of tide-induced melt, but may restrict our model's capacity to predict absolute basal melt rates. The crosses in Figure 6c show the estimated increase in melt rate due to tides based on Equation 20.

4. Discussion

4.1. Insights Into Melt Rate Sensitivity to Tide-Induced Boundary Layer Mixing

Based on the assumption that tide-driven shear influences mixing beyond the pycnocline, we have shown that incorporating the effect of tides into a one-dimensional model of ice shelf-ocean boundary current results in enhanced rates of basal melting and freezing. The simulated melt rate increase, which can be explained by enhanced turbulent transport of heat across the plume-ambient interface, imparts more buoyancy to the plume causing it to accelerate. The increase in plume speed further enhances entrainment of ambient water, which decreases the relative importance of tide-induced drag at the ice base. For cold ice shelves, this translates into a strengthening of the ice pump circulation, with amplified melting in the grounding zone, followed by increased freezing further along the plume path. The magnitude of these effects depends on a combination of factors that influence the level to which tidal currents dominate over the thermohaline-only plume circulation (i.e., local tidal current speeds, ambient ocean temperature, and ice shelf basal geometry).

It is important to emphasize that these findings are dependent on the approach chosen to incorporate the influence of tides into the model. For the purpose of this study, this consisted of incorporating a tidal contribution to the scalar turbulent transfer velocity formulations, momentum flux conservation equation, and entrainment rate expression. The first two modifications parameterize enhanced turbulent mixing of heat, salt, and momentum across the plume caused by tide-driven turbulence production at the ice-ocean interface. The increased turbulent transport of heat and salt translates into an enhanced plume layer diffusivity. On its own, this would result in increased heat flux across the ice-ocean interface and consequently increased melting (see blue dots in Figure 6b). The enhancement of turbulent mixing of momentum creates a counter-effect by inducing increased frictional drag, which slows down the plume. In the ice shelf configurations considered in this study, with the exception of Cosgrove, the retarding effect of tide-induced drag on the plume dynamics dominates. If entrainment was assumed to be unaffected by tidal currents this would lead to a decrease of heat flux across the ice-ocean interface. Due to the proportionality between melt rate and plume speed this would then translate into a relative reduction in melt rate due to tides (see orange dots in Figure 6b). However, based on a comparative study between the thickness of the simulated plume and a theoretical expression for tidal boundary layer thickness, we chose to incorporate tide-induced entrainment. With this set up our simulations suggest that the increase in plume speed due to tide-driven turbulent heat transport across the pycnocline dominates over the deceleration due to tide-induced friction at the ice base. As a result, the melt rate increases, causing the boundary current to accelerate, which acts to increase melting further (see green dots in Figure 6b).

Despite the simplified representation of sub-ice shelf ocean dynamics in the 1-D model used here, our results qualitatively agree with those documented in previous 3-D ocean modeling studies, where the explicit inclusion of tidal currents was generally reported to strengthen the cavity circulation and increase rates of basal melting and freezing (e.g., Arzeno et al., 2014; Gwyther et al., 2016; Makinson et al., 2011; Mueller et al., 2018; Robertson, 2013). However, as previously mentioned, our model only simulates boundary current processes whereas the aforementioned studies also took into account large-scale tidal processes responsible for modifying

water masses entering the ice shelf cavity, and hence reported the combined effect of these mechanisms on basal melt. Without the ability to distinguish the influence of the individual tidal processes, it is not possible to establish how the effects of tides predicted by our model compare with those simulated by the tide-resolving models mentioned above. By contrast, Jourdain et al. (2019) and Hausmann et al. (2020) applied a decomposition technique to differentiate between changes in basal melt due to boundary current processes and changes induced by tidal mechanisms occurring away from the ice shelf base. Their analyses suggest that tides act to increase net basal melt rates, and that this change is primarily driven by enhanced turbulent heat fluxes at the ice-ocean interface. In line with these studies, an increase in melt rates was obtained when adding tides into the plume model based on Equations 14–17. However, our results suggests that the simulated increase in melt is mainly caused by enhanced turbulent mixing across the outer edge of the plume (as indicated by the increase in plume temperature due to entrainment along melting portions of the plume path). While this finding may only be relevant from a qualitative point of view due to the simplicity of our model, it nevertheless highlights the critical importance of the representation of tide-induced mixing across the pycnocline when estimating melt rates in the presence of tides.

While improving the representation of turbulent fluxes at the ice-ocean interface has been the focus of many recent modeling and observational studies (e.g., Dansereau & Losch, 2013; Rosevear et al., 2022), the processes controlling the vertical transport of heat from the ambient waters into the boundary current are not yet well understood. For models in which turbulent mixing across the pycnocline is unresolved, like the plume model employed in this study, this uncertainty means that the representation of the entrainment process relies on choosing between one of many proposed parameterizations that each vary substantially in terms of predicted entrainment rates (Burchard et al., 2022). More sophisticated 3-D ocean models with sufficiently high resolution may not depend on entrainment parameterizations, but they typically employ generic vertical mixing schemes that are not necessarily accurate for the sub-ice shelf environment and that may respond differently to the addition of tides. This latter point is highlighted by the large range of estimated tide-induced melt rates obtained from 3-D ocean circulation models of the same ice shelf (e.g., Hausmann et al. (2020) and Mueller et al. (2018) for Filchner-Ronne). Both models applied similar parameterizations of heat and salt transfer across the ice-ocean interface but they employed different vertical mixing schemes. Despite other modeling set up differences (e.g., in the external forcing), this suggests that the variations in simulated tide-driven melt rates can at least partially be attributed to the differing responses of the implemented mixing schemes to the incorporation of tides into the model. The influence that the gaps in our understanding of the entrainment mechanism can have on conclusions drawn from numerical studies supports the need for current measurements across the complete ice shelf-ocean boundary flow and particularly across the pycnocline.

4.2. Accounting for Tide-Induced Mixing in Basal Melt Rate Parameterizations

One of the motivations behind this study was to use the insights gained from the plume model simulations to provide suggestions on how to account for tide-induced basal melting in standalone ice sheet models that rely on parameterizations to estimate ocean-driven melt. The most accurate approach would be to follow the analysis presented by L2019 to construct a new melt rate approximation from the plume model equations with modified formulations of the turbulent transfer velocities, plume conservation equation, and entrainment expression as per Equations 14–17 to account for the presently neglected effects of tide-induced mixing. However, incorporating a spatially varying U_t into the analytical derivation would be difficult to implement. Alternatively, a possible approach would consist in computing melt rates based on the original L2019 expression and then applying an enhancement factor calculated as per Equation 20 based on a cavity-integrated ratio of characteristic tidal current magnitude to thermohaline-only plume velocity.

A range of Antarctic ice shelf basal geometries were considered to derive Equation 20. Nevertheless, it should be applied with caution due to limitations associated with the use of the one-dimensional plume model from which the relationship was derived. More specifically, due to its single horizontal dimension the model does not capture cross-slope gradients or other factors related to Earth's rotation such as the asymmetry of the cavity circulation (Rosevear et al., 2022). Second, the lack of vertical structure within the plume means that the effect of boundary current stratification on plume dynamics is neglected (Jenkins, 2016) and that parameterized dynamical processes such as entrainment are based on bulk properties of the plume. Furthermore, the influence of ambient ocean stratification on plume dynamics (Bradley et al., 2022) has been neglected and we do not consider the

potential effect that different ambient ocean salinity values would have on entrainment. Finally, as discussed in previous sections, the approximation given in Equation 20 is only valid under the assumption that tide-induced shear at the ice-ocean interface impacts mixing beyond the depth of the pycnocline. It should also be noted that, similarly to the standard approach consisting in tuning coefficients to match observed melt rates (e.g., Burgard et al., 2022), applying a melt rate offset based on Equation 20 would imply that the relative change in melting due to tides does not vary along the ice base. Since tide-induced melt rates were found to depend on local tidal current strength and local slope, the application of a uniform tide-induced melt rate might bias the prediction of melt rate distribution patterns. However, based on the conclusions of recent study suggesting a minor sensitivity of modeled ice loss to basal melt distribution (Joughin et al., 2021), this bias might be acceptable within the context of ice sheet modeling.

While the approach proposed above might allow for a representation of the effect of tide-induced turbulence on basal melt rates in models that do not resolve tides, parameterizing the effect of tides in this way would imply that tidal currents solely impact melt rates through turbulent boundary layer processes. This might be the case under certain ice shelves in the Weddell Sea and Amundsen Sea sectors (Hausmann et al., 2020; Jourdain et al., 2019), but a recent modeling effort based on a pan-Antarctic simulation (Richter et al., 2022) highlighted large regional variations in terms of the mechanisms by which tides modulate basal melt. This emphasizes the importance of applying the tide-induced melt rate parameterization proposed here in conjunction with other parameterizations to account for basal melt rate modulations introduced by other processes like tidal vertical mixing and residual circulation (e.g., Makinson, 2002).

5. Conclusion

We present a sensitivity analysis of the impact of tide-induced turbulence on ice shelf basal melt rates based on the theory of subglacial plumes. It was done by incorporating tidal current effects into the one-dimensional plume model of Jenkins (1991) evaluated with unstratified ambient ocean conditions, and the results should be interpreted in this context. Our simulations highlight that melt rates depend on the balance between turbulent mixing of heat and momentum across the ice-ocean interface and across the pycnocline (i.e., entrainment). By testing this balance, we have demonstrated that the direction of relative tide-induced basal melt depends on whether tide-driven shear at the ice-ocean interface is assumed to enhance mixing of ambient water into the plume. Based on a limited data set of 1-D idealized and realistic cross-sections representative of Antarctic ice shelves geometries, a quadratic relationship between the X-averaged tide-induced melt and the ratio of X-averaged tidal current magnitude to thermohaline-only plume speed was inferred. In the absence of a new plume parameterization of basal melt incorporating tide-induced mixing effects, this simple approximation could be used in applications in which basal melt rates need to be estimated without relying on ocean general circulation models (e.g., standalone ice sheet models).

Interesting areas of further research that would help to increase the robustness of the proposed parameterization would be to account for the effects of Earth's rotation and boundary current stratification by including the tide-induced turbulent mixing processes in a more sophisticated 2-D or 3-D model with sufficient vertical resolution to allow for the meltwater plume to be fully resolved. Finally, while previous observational campaigns have focused on improving the representation of turbulent processes at the ice-ocean interface (e.g., Davis & Nicholls, 2019), there has been less emphasis on quantifying the sources of TKE and their control on entrainment across the pycnocline. We acknowledge that in-situ current measurements beneath ice shelves are challenging to obtain. However, given the impact that contrasting theoretical assumptions can have on modeled tide-induced melt rates, obtaining current structure data across the ice shelf-ocean boundary current and beyond the pycnocline in cavities forced by strong tidal currents would be extremely valuable in terms of improving the predictions of Antarctic ice shelf melt rates, and hence sea level rise projections.

Appendix A: Comparison Between Plume Thickness and Theoretical Tidal Boundary Layer Thickness

In order to evaluate whether or not to incorporate tides into the entrainment parameterization, the plume thickness obtained from the model simulations was compared with a theoretical tidal boundary layer thickness calculated based on Equation 19. More detail on the interpretation of Figure A1 can be found in Section 3.3.

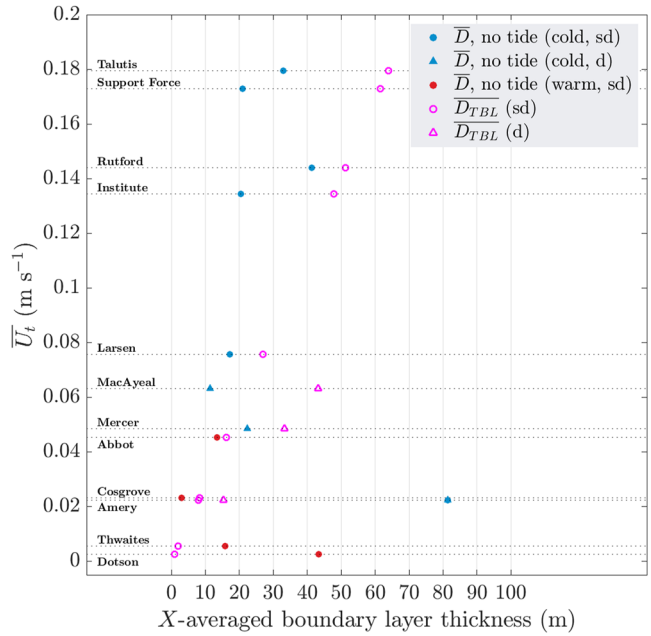

Figure A1. *X*-averaged plume thickness and theoretical tidal boundary layer thickness for the Realistic flowlines (Figure 2). Solid markers indicate results obtained from the plume model simulations (blue = cold cavity; red = warm cavity). Pink unfilled markers indicate theoretical tidal boundary layer thickness calculated as per Equation 19 based on the location specific *X*-averaged tidal current speed (as indicated by the horizontal dashed lines). Circles indicate semi-diurnal tides, diamonds indicate diurnal tides.

Data Availability Statement

The map in Figure 2 was created using the Antarctic Mapping Tools toolbox (Greene et al., 2017) available on Github https://github.com/chadagreene/Antarctic-Mapping-Tools. For the same figure, flowline coordinates and ice speed data were obtained from the MEaSUREs InSAR-Based Antarctica Ice Velocity Map, Version 2 data set (Mouginot et al., 2012, 2017) available via doi: https://doi.org/10.5067/D7GK8F5J8M8R and basal melt rate data was obtained from Adusumilli et al. (2020b) which can be found at https://library.ucsd.edu/dc/collection/bb0175934d. Ice shelf profile data (ice base, water column thickness) for the Realistic flowlines was obtained from the MEaSUREs BedMachine Antarctic, Version 2 data set (Morlighem, 2020), which can be accessed via doi: https://doi.org/10.5067/E1QL9HFQ7A8M. Tidal current data for the Realistic experiment was obtained from the regional barotropic tide model CATS2008 (Howard et al., 2019), an update to the model described by Padman et al. (2002), available for download through the U.S. Antarctic Program Data Center via doi: https://doi.org/10.15784/601235. The model was accessed using the Tide Model Driver version 2.5, Toolbox for Matlab (Erofeeva et al., 2020) available on Github. Coordinates for the selected flowlines and model outputs used to generate the figures are available at https://github.com/josephineanselin/plumemodeldata.

Acknowledgments
B.C.R. is supported by an ENVISION Doctoral Training Partnership studentship from the Natural Environment Research Council. J.A. is supported by a C-CLEAR Doctoral Training Partnership studentship from the Natural Environmental Research Council. We would also like to thank Carolyn B. Begeman, Madelaine G. Rosevear and Tyler Pelle for their thorough review and helpful comments which greatly improved the quality of the manuscript.

References

Adusumilli, S., Fricker, H. A., Medley, B., Padman, L., & Siegfried, M. R. (2020a). Interannual variations in meltwater input to the Southern Ocean from Antarctic ice shelves. *Nature Geoscience*, *13*(9), 616–620. https://doi.org/10.1038/s41561-020-0616-z

Adusumilli, S., Fricker, H. A., Medley, B. C., Padman, L., & Siegfried, M. R. (2020b). Data from: Interannual variations in meltwater input to the Southern Ocean from Antarctic ice shelves. [Dataset]. UC San Diego Library Digital Collections. https://doi.org/10.6075/J04Q7SHT

Arzeno, I., Beardsley, R. C., Limeburner, R., Owens, B., Padman, L., Spring, S. R., et al. (2014). Ocean variability contributing to basal melt rate near the ice front of Ross Ice Shelf, Antarctica. *Journal of Geophysical Research: Oceans*, *119*(7), 8410–8421. https://doi.org/10.1002/2014JC009792.Received

Asay-Davis, X. S., Jourdain, N. C., & Nakayama, Y. (2017). Developments in simulating and parameterizing interactions between the southern ocean and the Antarctic ice sheet. *Current Climate Change Reports*, *3*(4), 316–329. https://doi.org/10.1007/s40641-017-0071-0

Bombosch, A., & Jenkins, A. (1995). Modeling the formation and deposition of frazil ice beneath Filchner-Ronne Ice Shelf. *Journal of Geophysical Research*, *100*(C4), 6983–6992. https://doi.org/10.1029/94jc03224

Bowden, K. F. (1978). Physical problems of the benthic boundary layer. (Tech. Rep.).

Bradley, A. T., Rosie Williams, C., Jenkins, A., & Arthern, R. (2022). Asymptotic analysis of subglacial plumes in stratified environments. *Proceedings of the Royal Society A: Mathematical, Physical and Engineering Sciences*, *478*(2259), 20210846. https://doi.org/10.1098/rspa.2021.0846

Burchard, H., Bolding, K., Jenkins, A., Losch, M., Reinert, M., & Umlauf, L. (2022). The vertical structure and entrainment of subglacial melt water plumes. *Journal of Advances in Modeling Earth Systems*, *14*(3), e2021MS002925. https://doi.org/10.1029/2021ms002925

Burgard, C., Jourdain, N. C., Reese, R., Jenkins, A., & Mathiot, P. (2022). An assessment of basal melt parameterisations for Antarctic ice shelves. https://doi.org/10.5194/tc-2022-32

Craven, M., Allison, I., Fricker, H. A., & Warner, A. R. (2009). Properties of a marine ice layer under the amery ice shelf, East Antarctica. *Journal of Glaciology*, *55*(192), 717–728. https://doi.org/10.3189/002214309789470941

Dansereau, H. P., Veronique, & Losch, M. (2013). Simulation of subice shelf melt rates in a general circulation model: Velocity-dependent transfer and the role of friction. *Journal of Geophysical Research: Oceans*, *2001*(3805), 1–26. https://doi.org/10.1002/2013JC008846.Received

Davis, P. E., & Nicholls, K. W. (2019). Turbulence observations beneath Larsen C ice shelf, Antarctica. *Journal of Geophysical Research: Oceans*, *124*(8), 5529–5550. https://doi.org/10.1029/2019JC015164

DeConto, R. M., & Pollard, D. (2016). Contribution of Antarctica to past and future sea-level rise. *Nature*, *531*(7596), 591–597. https://doi.org/10.1038/nature17145

Erofeeva, S., Padman, L., & Howard, S. L. (2020). *Tide model driver (TMD) toolbox for Matlab*. Github. Retrieved from https://www.github.com/EarthAndSpaceResearch/TMD_Matlab_Toolbox_v2.5

Favier, L., Jourdain, N. C., Jenkins, A., Merino, N., Durand, G., Gagliardini, O., et al. (2019). Assessment of sub-shelf melting parameterisations using the ocean-ice-sheet coupled model NEMO(v3.6)-Elmer/Ice(v8.3). *Geoscientific Model Development*, *12*(6), 2255–2283. https://doi.org/10.5194/gmd-12-2255-2019

Galton-Fenzi, B. K., Hunter, J. R., Coleman, R., Marsland, S. J., & Warner, R. C. (2012). Modeling the basal melting and marine ice accretion of the Amery Ice Shelf. *Journal of Geophysical Research*, *117*(9), 1–20. https://doi.org/10.1029/2012JC008214

Greene, C. A., Gwyther, D. E., & Blankenship, D. D. (2017). Antarctic Mapping Tools for Matlab. *Computers & Geosciences*, *104*, 151–157. https://doi.org/10.1016/j.cageo.2016.08.003

Gudmundsson, G. H., Paolo, F. S., Adusumilli, S., & Fricker, H. A. (2019). Instantaneous Antarctic ice sheet mass loss driven by thinning ice shelves. *Geophysical Research Letters*, *46*(23), 13903–13909. https://doi.org/10.1029/2019GL085027

Gwyther, D. E., Cougnon, E. A., Galton-Fenzi, B. K., Roberts, J. L., Hunter, J. R., & Dinniman, M. S. (2016). Modelling the response of ice shelf basal melting to different ocean cavity environmental regimes. *Annals of Glaciology*, *57*(73), 131–141. https://doi.org/10.1017/aog.2016.31

Hausmann, U., Sallée, J. B., Jourdain, N. C., Mathiot, P., Rousset, C., Madec, G., et al. (2020). The role of tides in ocean-ice shelf interactions in the southwestern Weddell Sea. *Journal of Geophysical Research: Oceans*, *125*(6), 1–29. https://doi.org/10.1029/2019JC015847

Hewitt, I. J. (2020). Subglacial plumes. *Annual Review of Fluid Mechanics*, *52*(1), 145–169. https://doi.org/10.1146/annurev-fluid-010719-060252

Holland, D. M., & Jenkins, A. (1999). Modeling thermodynamic ice-ocean interactions at the base of an ice shelf. *Journal of Physical Oceanography*, *29*(8)(8 PART 1), 1787–1800. https://doi.org/10.1175/1520-0485(1999)029⟨1787:mtioia⟩2.0.co;2

Holland, D. M., & Jenkins, A. (2001). Adaptation of an isopycnic coordinate ocean model for the study of circulation beneath Ice Shelves. *Monthly Weather Review*, *129*(8), 1905–1927. https://doi.org/10.1175/1520-0493(2001)129<1905:aoaico>2.0.co;2

Holland, P. R., & Feltham, D. L. (2006). The effects of rotation and ice shelf topography on frazil-laden ice shelf water plumes. *Journal of Physical Oceanography*, *36*(12), 2312–2327. https://doi.org/10.1175/JPO2970.1

Holland, P. R., Jenkins, A., & Holland, D. M. (2008). The response of Ice shelf basal melting to variations in ocean temperature. *Journal of Climate*, *21*(11), 2558–2572. https://doi.org/10.1175/2007JCLI1909.1

Howard, S. L., Erofeeva, S., & Padman, L. (2019). CATS2008: Circum-Antarctic tidal simulation version 2008. [Software]. U.S. Antarctic Program (USAP) Data Center. Retrieved from https://www.esr.org/research/polar-tide-models/list-of-polar-tide-models/cats2008/

Jenkins, A. (1991). A one dimensional model of ice-ocean interaction. *Journal of Geophysical Research*, *96*(Cll), 671–677. https://doi.org/10.1029/91JC01842

Jenkins, A. (2011). Convection-driven melting near the grounding lines of ice shelves and tidewater glaciers. *Journal of Physical Oceanography*, *41*(12), 2279–2294. https://doi.org/10.1175/JPO-D-11-03.1

Jenkins, A. (2016). A simple model of the ice shelf-ocean boundary layer and current. *Journal of Physical Oceanography*, *46*(6), 1785–1803. https://doi.org/10.1175/JPO-D-15-0194.1

Jenkins, A. (2021). Shear, stability and mixing within the ice shelf-ocean boundary current. *Journal of Physical Oceanography*, 2129–2148. https://doi.org/10.1175/jpo-d-20-0096.1

Jenkins, A., Nicholls, K. W., & Corr, H. F. (2010). Observation and parameterization of ablation at the base of Ronne ice Ahelf, Antarctica. *Journal of Physical Oceanography*, *40*(10), 2298–2312. https://doi.org/10.1175/2010JPO4317.1

Jenkins, A., Shoosmith, D., Dutrieux, P., Jacobs, S., Kim, T. W., Lee, S. H., et al. (2018). West Antarctic Ice Sheet retreat in the Amundsen Sea driven by decadal oceanic variability. *Nature Geoscience*, *11*(10), 733–738. https://doi.org/10.1038/s41561-018-0207-4

Joughin, I., Alley, R. B., & Holland, D. M. (2012). Ice-sheet response to oceanic forcing. *Science*, *338*(6111), 1172–1176. Retrieved from http://science.sciencemag.org/content/sci/338/6111/1172.full.pdf

Joughin, I., Shapero, D., Dutrieux, P., & Smith, B. (2021). Ocean-induced melt volume directly paces ice loss from Pine Island Glacier. *Science Advances*, *7*(43). https://doi.org/10.1126/sciadv.abi5738

Jourdain, N. C., Molines, J. M., Le Sommer, J., Mathiot, P., Chanut, J., de Lavergne, C., & Madec, G. (2019). Simulating or prescribing the influence of tides on the Amundsen Sea ice shelves. *Ocean Modelling*, *133*(October 2018), 44–55. https://doi.org/10.1016/j.ocemod.2018.11.001

Lambrecht, A., Sandhäger, H., Vaughan, D. G., & Mayer, C. (2007). New ice thickness maps of Filchner-Ronne Ice Shelf, Antarctica, with specific focus on grounding lines and marine ice. *Antarctic Science*, *19*(4), 521–532. https://doi.org/10.1017/S0954102007000661

Lazeroms, W. M., Jenkins, A., Rienstra, S. W., & Van De Wal, R. S. (2019). An analytical derivation of ice-shelf basal melt based on the dynamics of meltwater plumes. *Journal of Physical Oceanography*, *49*(4), 917–939. https://doi.org/10.1175/JPO-D-18-0131.1

Lewis, E. L., & Perkin, R. G. (1986). Ice pumps and their rates. Tech. Rep. (Vol. *91*).

Little, C. M., Gnanadesikan, A., & Oppenheimer, M. (2009). How ice shelf morphology controls basal melting. *Journal of Geophysical Research*, *114*(12), 1–15. https://doi.org/10.1029/2008JC005197

Makinson, K. (2002). Modeling tidal current profiles and vertical mixing beneath Filchner-Ronne Ice Shelf, Antarctica. *Journal of Physical Oceanography*, *32*(1), 202–215. https://doi.org/10.1175/1520-0485(2002)032⟨0202:MTCPAV⟩2.0.CO;2

Makinson, K., Holland, P. R., Jenkins, A., Nicholls, K. W., & Holland, D. M. (2011). Influence of tides on melting and freezing beneath Filchner-Ronne ice shelf, Antarctica. *Geophysical Research Letters*, *38*(6), 4–9. https://doi.org/10.1029/2010GL046462

Morlighem, M. (2020). MEaSUREs BedMachine Antarctica, version 2. [Dataset]. NASA National Snow and Ice Data Center Distributed Active Archive Center. https://doi.org/10.5067/E1QL9HFQ7A8M

Morlighem, M., Rignot, E., Binder, T., Blankenship, D., Drews, R., Eagles, G., et al. (2020). Deep glacial troughs and stabilizing ridges unveiled beneath the margins of the Antarctic ice sheet. *Nature Geoscience*, *13*(2), 132–137. https://doi.org/10.1038/s41561-019-0510-8

Mouginot, J., Rignot, E., Scheuchl, B., & Millan, R. (2017). Comprehensive annual ice sheet velocity mapping using Landsat-8, Sentinel-1, and RADARSAT-2 data. *Remote Sensing*, *9*(4), 364. https://doi.org/10.3390/rs9040364

Mouginot, J., Scheuch, B., & Rignot, E. (2012). Mapping of ice motion in Antarctica using synthetic-aperture radar data. *Remote Sensing*, *4*(9), 2753–2767. https://doi.org/10.3390/rs4092753

Mueller, R. D., Hattermann, T., Howard, S. L., & Padman, L. (2018). Tidal influences on a future evolution of the Filchner-Ronne ice shelf cavity in the Weddell Sea, Antarctica. *The Cryosphere*, *12*(2), 453–476. https://doi.org/10.5194/tc-12-453-2018

Mueller, R. D., Padman, L., Dinniman, M. S., Erofeeva, S. Y., Fricker, H. A., & King, M. A. (2012). Impact of tide-topography interactions on basal melting of Larsen C Ice Shelf, Antarctica. *Journal of Geophysical Research*, *117*(5), 1–20. https://doi.org/10.1029/2011JC007263

Nicholls, K. W., Østerhus, S., Makinson, K., Gammelsrød, T., & Fahrbach, E. (2009). Ice-ocean processes over the continental shelf of the southern Weddell Sea. *Antarctica: A review*, *47*(3), RG3003. https://doi.org/10.1029/2007RG000250

Padman, L., Fricker, H. A., Coleman, R., Howard, S., & Erofeeva, L. (2002). A new tide model for the Antarctic ice shelves and seas. *Annals of Glaciology*, *34*, 247–254. https://doi.org/10.3189/172756402781817752

Padman, L., Siegfried, M. R., & Fricker, H. A. (2018). Ocean tide influences on the Antarctic and Greenland ice sheets. *Reviews of Geophysics*, *56*(1), 142–184. https://doi.org/10.1002/2016RG000546

Paolo, F. S., Fricker, H. A., & Padman, L. (2015). Volume loss from Antarctic ice shelves is accelerating. *Science*, *348*(6232), 327–331. https://doi.org/10.1126/science.aaa0940

Pederson, B. (1980). Dense bottom currents in rotating ocean. *Journal of the Hydraulics Division*, *106*(8), 1291–1308. https://doi.org/10.1061/jyceaj.0005481

Richter, O., Gwyther, D. E., King, M. A., & Galton-Fenzi, B. K. (2022). The impact of tides on Antarctic ice shelf melting. *The Cryosphere*, *16*(4), 1409–1429. https://doi.org/10.5194/tc-16-1409-2022

Rignot, E., Mouginot, J., & Scheuchl, B. (2011). Ice flow of the Antarctic ice sheet. *Science*, *333*(6048), 1423–1427. https://doi.org/10.1126/science.1207922

Rignot, E., Mouginot, J., & Scheuchl, B. (2017). MEaSUREs InSAR-based Antarctica ice velocity map, version 2. [Dataset]. NASA National Snow and Ice Data Center Distributed Active Archive Center. https://doi.org/10.5067/D7GK8F5J8M8R

Robertson, R. (2013). Tidally induced increases in melting of Amundsen Sea ice shelves. *Journal of Geophysical Research: Oceans*, *118*(6), 3138–3145. https://doi.org/10.1002/jgrc.20236

Rosevear, M., Galton-Fenzi, B., & Stevens, C. (2022). Evaluation of basal melting parameterisations using in situ ocean and melting observations from the Amery Ice Shelf, East Antarctica. *Ocean Science*, *18*(4), 1109–1130. https://doi.org/10.5194/os-18-1109-2022

Smedsrud, L. H., & Jenkins, A. (2004). Frazil ice formation in an ice shelf water plume. *Journal of Geophysical Research*, *109*(3), 1–15. https://doi.org/10.1029/2003jc001851